

Neuro-Modeling Infused EMT Analytics

Qing Shen, *Graduate Student Member, IEEE*, Yifan Zhou, *Member, IEEE*, Peng Zhang, Yacov A. Shamash, *Fellow, IEEE*, Xiaochuan Luo, *Senior Member, IEEE*, Bin Wang, *Senior Member, IEEE*, Huanfeng Zhao, *Member, IEEE*, Roshan Sharma, *Member, IEEE*, Bo Chen, *Member, IEEE*

Abstract—The paper presents a systematic approach to developing Physics-Informed neuro-Models (PIM) for the transient analysis of power grids interconnected with renewables. PIM verifies itself as an adequate digital twin of power components, taking full advantage of physical constraints while requiring only a small fraction of data for training. Three new contributions are presented: 1) An PINN-enabled neuro-modeling approach is devised to construct an accurate EMT model; 2) A data-physics hybrid learning approach is substantiated to demonstrate its data efficiency and adaptability at various levels of data; 3) A balanced-adaptive PIM exemplifies its applicability when multiple terms are predicted simultaneously while maintaining alignment with physical principles. Under various operational scenarios, tests on rotating and static electric components as well as an IEEE test system verify the efficacy and efficiency of the new learning-infused transient grid analytics.

Index Terms—EMT modeling, inverter-based resources, physics-informed machine learning, self-adaptive learning, data-physics hybrid learning, induction machine

I. INTRODUCTION

ELECTROMAGNETIC Transients [1] (EMT) simulations, capable of capturing high-fidelity fast dynamics are indispensable for the planning and operation of today’s digitally controlled and distributed power grid progressively dominated by inverter-based resources (IBRs) and renewables. Accurately representing fast dynamics under possible scenarios are of critical importance for the resilient interconnection of distributed energy resources (DERs) into the associated grids [2]. However, modeling the power electronic switching of inverters and the associated controls requires highly complex component models and extremely small simulation time steps [3].

As a resolution, data-driven modeling has been investigated to address these long-standing challenges [4], [5]. Data-driven machine learning, however, requires high-quality real-time data. In today’s power grids, acquiring such metadata sets for abnormal situations is challenging, given that customers tend to preserve their data privacy and that abnormal events suitable for training purposes are unlikely to occur [6]. Even when datasets for these rare events can be obtained through

simulations, they significantly increase computational burdens and storage expenses [7]. Another challenge arises when facing diversified operations; the neural network learned from data needs to be repeatedly retrained to be generalizable [8].

To address the limitations of data availability and compromised generalization, a new trend in scalable dynamic modeling is to exploit transformative physics-informed machine learning techniques [9]–[12] to circumvent the drawbacks of conventional purely data-driven modeling for IBR interconnected grids. The key idea of this paper is to establish an architecture where the transient behaviors of a grid are captured by infusing EMT modeling with learning-based component models which can essentially streamline the process for solving differential equations of these grid components [13], [14]. This is expected to result in more tractable EMT computations, achieving model plug-and-plays while maintaining simulation accuracy.

Nevertheless, two obstacles persist in the implementation of PINNs. While they are data-efficient, PINNs can not be entirely data-free as complex grids can exhibit significantly different behaviors with slight parameter changes [15]. Periodic synchronization with measurement data is essential to keep the learned twin model aligned with reality [16]. Therefore, hybrid learning enhanced with data is necessitated. Additionally, unlike conventional data-driven training, the loss function in PINNs often involves multiple terms corresponding to sets of physical equations such as Ordinary Differential Equations (ODE) or Differential Algebraic Equations (DAE). Determining how to allocate weights for each physical term remains an open problem [17], [18].

This paper addresses the bottlenecks of PINN—hybrid learning and training weights allocation—to enable learning-infused transient grid analytics. We propose a systematic approach to establishing a component-based full-order Physics-Informed neuro-Model (PIM) as a high-fidelity digital twin that reflects the states of its corresponding physical counterpart. It learns from historical data, adheres to the physical model, and makes predictions using real-time data. The contributions of PIM are threefold:

- A PINN-enabled neuro-modeling method is devised to construct an accurate EMT model for perturbed power system components, leveraging physical knowledge. This approach effectively adapts to parameter changes and scenarios with limited or low-quality data.
- A data-physics hybrid learning approach is established, which is enhanced and updated with data, to generate robust and accurate fast and slow dynamics with varying levels of data.

This work was supported in part by the National Science Foundation under Grant No. ITE-2134840 and in part by ISO New England. This work relates to the Department of Navy award N00014-24-1-2287 issued by the Office of Naval Research. The U.S. Government has a royalty-free license throughout the world in all copyrightable material contained herein.

Q. Shen, Y. Zhou, P. Zhang, Y. A. Shamash and H. Zhao are with the Department of Electrical and Computer Engineering, Stony Brook University, NY, USA (e-mails: qing.shen, yifan.zhou.1, p.zhang, yacov.shamash@stonybrook.edu, huanfengzhao@gmail.com).

X. Luo and B. Wang are with ISO New England, Holyoke, MA, USA (e-mails: xluo, bwang@iso-ne.com).

R. Sharma and B. Chen are with Commonwealth Edison, Chicago, IL, USA (e-mails: roshan.sharma, bo.chen@comed.com).

- A balanced-adaptive learning strategy is devised and substantiated, which presents itself as a lightweight yet efficient method for weight allocation when predicting multiple terms simultaneously.

The aforementioned contributions lay a solid foundation for learning-infused transient grid analytics which has been extensively validated in both dynamic components modeling and accurate EMT simulations of an IEEE test system.

II. ENHANCED PHYSICS-INFORMED NEURAL MODELING

In this section, we present two approaches to enhancing PINN for EMT analytics: data-physics hybrid learning of power system components and balanced-adaptive physics-informed learning.

A. Preliminaries of physics-informed learning

This subsection briefly introduces the background knowledge of PINN and highlights its advantages over purely data-driven approaches.

Consider a system of ordinary differential equations with a state vector u and a parameter vector γ :

$$\begin{aligned} \frac{du}{dt} &= R(u, \gamma), \quad u|_{t=0} = u_0 \\ y &= f(\dot{u}, u, \gamma) \end{aligned} \quad (1)$$

where R, f represents the governing physical laws. Consider a machine learning task to learn a neural network u_{NN} to represent the solution of (1), i.e., the trajectory of $u(t)$ under arbitrary given γ and u_0 :

$$u(t) = u_{NN}(u_0, \gamma) \quad (2)$$

Conventional data-driven machine learning directly computes the loss function by the differences between the predictions from the neural network and the training data (denoted by \tilde{u}):

$$L_{data} = \text{mean}(\|\tilde{u} - u_{NN}\|_2) \quad (3)$$

However, such a data-driven learning architecture demands abundant accurate training data, underscoring the need for both data quality and quantity to address diverse scenarios.

In contrast, PINN leverages the physical constraints in (1) to necessitate the alignment of the predicted outputs u_{NN} with the inherent physical equations, contributing to a physics-informed loss function elaborated below:

$$L_{physics} = \text{mean}\left(\left\|\frac{du_{NN}}{dt} - R(u_{NN}, \gamma)\right\|_2\right) \quad (4)$$

Comparing L_{data} and $L_{physics}$, an obvious distinction is that PINN exploits the inherent physical laws in (1), to construct the loss function. Through the minimization of this physics-informed loss, the prediction from the neural network is compelled to conform to the real states of the physical system, thus significantly reducing the dependency on extensive high-quality datasets.

B. Data-physics hybrid learning of power system component

One complication of the purely physics-informed method is that it requires many iterations to get converged, especially for fast transient cases [19]. Interestingly, even if a small amount of data is available, the efficiency of training is found to be extensively improved [20]. Physics-informed learning enhanced with data can turn a neural network into a fast learner. Besides, it is sometimes unrealistic to derive the perfect first principle equation. Therefore, a data-physics hybrid PIM is proposed to unlock the potential.

Hybrid learning can be regarded as a grey box with a compelling advantage that, provided only limited data to equip with the training, exhibits a notable generalization ability that may surpass what the purely data-driven approach requires significantly more data. In contrast, data-driven neural networks may suffer from overfitting or underfitting obstacles if the dataset is incomplete or insufficient [13]. Hybrid PIM thus ignites the hope to make up for the incomplete data set by deploying physics information.

Suppose a power system component is to be described as a set of differential-algebraic equations as in (1). Substitute the neural network u_{NN} in (2) to (1):

$$\begin{aligned} \frac{du_{NN}}{dt} &= R(u_{NN}, \gamma), \quad u|_{t=0} = u_0 \\ \hat{y} &= f(\dot{u}_{NN}, u_{NN}, \gamma) \end{aligned} \quad (5)$$

Then one or a series of neural networks can be used to learn the dynamic models of this component. A specially designed framework for the power system components is illustrated in Fig. 1, where the framework function in the dashed-line box stands for intermediate functions before entering the next neural network. For example, if the component being learned is a rotating device such as an induction machine, the framework function can be a Park transformation. A more detailed modeling will be discussed in Subsection III-A. The n networks can be learned in parallel or series. Each construction of the loss function fully exploits the physical equations.

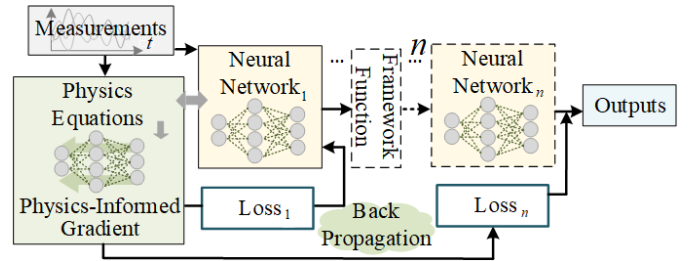


Fig. 1: Schematic diagram of PIM: a physics-informed, multi-neural network structure.

For hybrid PIM learning, the construction of loss is defined as:

$$\mathcal{L} = \min_{\delta} L_{hybrid} = \min_{\delta} (L_{physics} + \eta L_{data}) \quad (6)$$

where δ is the parameters of the neural networks; η is the percentage of data acquisition, which depends on the data availability.

C. Balanced-adaptive physics-informed learning

Once the data level η in (6) is established, another challenge emerges in formulating an effective loss function within $L_{physics}$.

Existing work in [21] proposes a loss scaling method to resolve the training difficulty. But its scaling is fixed during the whole training. In [22], they enhance the collocation point set via an auxiliary neural network. In [23], a sequential training strategy is introduced to remedy the violation of temporal causality during model training. Nevertheless, its loss calculation relies on the previous time steps, introducing an extra iteration per epoch, significantly increasing computational complexity. Moreover, these intricate methods have primarily addressed low-dimensional problems; whereas in power systems, the involved dimensions are usually higher, either sequential casual training or auxiliary network approaches introduce extra training burdens and are prone to convergence difficulties.

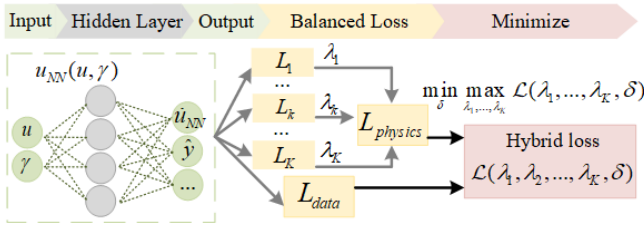


Fig. 2: Schematic diagram of the BA-loss for streamlined PIM.

We propose a balanced and adaptive physics-informed loss (BA-loss) to tackle the challenge of formulating the high-dimensional loss terms in $L_{physics}$ (see Fig. 2). Suppose the learning encompasses K physical loss terms L_1, L_2, \dots, L_K with $\lambda_1, \lambda_2, \dots, \lambda_K$ as their weights. The challenge lies in the fact that the range of each loss term in $L_{physics}$ is different since each term represents a realistic physical meaning. Thus, it is complicated to identify a set of proper weights to balance different loss terms. In conventional PINN algorithms, those weights are pre-defined and manually tuned, which is, as aforementioned, inefficient and ineffective. In the proposed balanced and adaptive loss, these weights can be defined as learnables that are automatically optimized during the learning process.

To begin with, the effect of each physical term needs to be balanced into the same range as:

$$L_{physics} = \frac{\sum_{k=1}^K \lambda_k L_k}{\max_k(L_k)} \quad (7)$$

Without this step, further optimization will be infeasible in training. Then the loss is optimized in a self-supervised manner that ascends in the loss weight space and descends in the model parameter space:

$$\min_{\delta} \max_{\lambda_1, \lambda_2, \dots, \lambda_K} \mathcal{L}(\delta, \lambda_1, \lambda_2, \dots, \lambda_K) \quad (8)$$

The learnables λ are clamped to be bigger than zero. The gradient descent of Balanced-adaptive (BA)-PIM is as follows:

$$\begin{aligned} \delta &\leftarrow \delta - \nabla_{\delta} \mathcal{L}(\delta, \lambda_1, \lambda_2, \dots, \lambda_K) \\ \lambda_k &\leftarrow \lambda_k + \nabla_{\lambda_k} \mathcal{L}(\delta, \lambda_1, \lambda_2, \dots, \lambda_K), \quad \forall k \end{aligned} \quad (9)$$

where

$$\nabla_{\lambda_k} \mathcal{L}(\delta, \lambda_1, \lambda_2, \dots, \lambda_K) = \frac{L_k}{\max_k(L_k)} \quad (10)$$

By constraint, $\lambda_k > 0$. $\nabla_{\lambda_k} \geq 0$ and is zero if and only if the corresponding physical term L_k is 0, e.g. $\nabla_{\lambda_k} \mathcal{L} = 0 \iff L_k = 0$. The learnable weights become larger if the corresponding physical losses are larger, progressively functioning as a faithful penalty on the network for not closely fitting the physical constraints. The diagram of the BA-PIM is shown in Fig. 2.

III. LEARNING-BASED TRANSIENTS MODELING FOR REPRESENTATIVE COMPONENTS

As discussed in Section II, the kernel of our PIM algorithm is the multi-neural network structure defined in Fig. 1 and the BA-enhanced physical loss defined in Fig. 2. In this section, we will demonstrate, given an arbitrary power system component, how to identify the best multi-neural network structure and the most efficient physical loss to learn the PIM.

Specifically, we showcase PIM on two important power system components, i.e., induction machines and inverters, which represent rotating components and static components, respectively.

A. Rotating component: induction machine

Without loss of generality, a typical yet important rotating component, the induction machine (IM) serves as a good example. For IMs, the optimal multi-neural network structure in Fig. 1 is to decompose the aforementioned data-physics hybrid learning into two lightweight neural networks, with the Park transformation as the connecting framework function between the two networks. The rationale behind this decomposition will be elaborated in Subsection III-A2.

IMs constitute a significant portion of loads, distributed energy resources (DERs), and industrial power systems. Among existing IM models, the voltage-behind-reactance (VBR) model is known for its interpretability and efficiency [24] [25]. Thus, this section combines PIM and VBR to develop a PIM-based Neural Induction Machine Model (NeuIM).

1) *Physical formulation of induction machine:* An induction machine can be represented as a set of differential algebraic equations. In the $dq0$ frame, the induction machine has two main parts [26]. First, for the electrical part, the voltage and flux linkage equations can be expressed as:

$$\begin{aligned} \dot{\lambda} &= \mathcal{S}(\lambda, \omega, \omega_r, i_{s,r}^{dq0}, v_s^{dq0}, r_{s,r}) \\ \lambda &= \mathcal{F}(i_{s,r}^{dq0}, L_{ls,lr}, L_M) \\ v_s^{dq0} &= \mathcal{J}(r_s, \omega, \lambda, i_s, \dot{\lambda}) \end{aligned} \quad (11)$$

where λ is the flux linkage; the subscript s denotes variables and parameters associated with the stator circuits, and subscript r denotes those from the rotor circuits, e.g., r_r is rotor resistance. $\mathcal{S}, \mathcal{F}, \mathcal{J}$ represent the physics laws governing the flux linkages. Current i^{dq0} , voltage v^{dq0} and flux linkage λ are in $dq0$ frame. Full details can be found in Appendix A. L_{ls}, L_{lr}, L_M are the stator, rotor, and mutual leakage inductance respectively.

However, the induction machine modeling in $dq0$ frame makes it difficult to integrate with the three-phase power grid directly [27] [28]. A traditional approach to obtaining the phase domain model from the $dq0$ model is through the mathematical derivation based on (11), and (29)-(33). But it is rather complicated as presented in Appendix A. As a solution, we propose a physics-informed, learning-based modeling approach that transforms the model from $dq0$ frame to the phase domain. PIM exhibits versatility and can be extended to various aspects, such as neural synchronous machines and neural transmission lines, extending beyond the scope of induction machines.

2) *Data-physics hybrid PIM-based induction machine:* When an IM is connected into a power system, it directly interacts with the system through the three-phase stator current (denoted as i_s^{abc}) and the terminal voltage (denoted as v_s^{abc}), rather than the $dq0$ frame states as shown in (11). Thus, the target is to identify an abc -phase model of the IM using PINN. We formulate the physics-informed neural model as:

$$\frac{di_s}{dt} = \mathcal{N}(v_s, z), \quad i_s|_{t=0} = i_0 \quad (12)$$

where v_s, i_s are in abc -frame, e.g., v_s^{abc}, i_s^{abc} for clarity. v_s is the terminal voltages on the stator side, \mathcal{N} is a neural network to predict the derivatives of i_s . i_0 is the initial values of i_s ; $[\theta, \omega, \omega_r]$ are denoted as z .

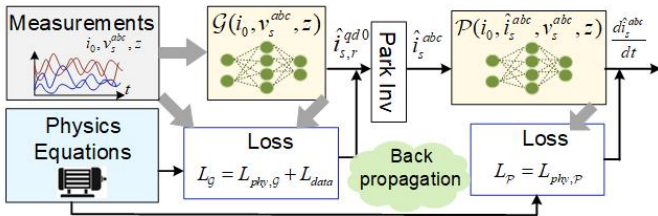


Fig. 3: Schematic diagram of PIM-based NeuIM.

As shown in Fig. 3, the kernel idea is to take advantage of the well-established physics equations of IM to learn the NeuIM model, i.e., \mathcal{N} in (12). Specifically, we divide \mathcal{N} into two sub-neural models \mathcal{G} and \mathcal{P} (see the yellow boxes in Fig. 3). The block \mathcal{G} learns the algebraic equations of the $dq0$ currents of the stator and the rotor (denoted as \hat{i}^{dq0}):

$$\hat{i}^{dq0} = \mathcal{G}(i_0, v_s, z) \quad (13)$$

Here the measurements z, v_s and initial values i_0 are the inputs of \mathcal{G} ; $\hat{\cdot}$ denotes the outputs from neural networks. Then \hat{i}_s (in abc frame) is obtained via Park's inverse transformation and passed into block \mathcal{P} , where \mathcal{P} will obtain the final output $d\hat{i}_s/dt$ in abc frame:

$$\frac{d\hat{i}_s}{dt} = \mathcal{P}(i_0, \hat{i}_s, v_s, z) \quad (14)$$

For rotating components, the decomposition of \mathcal{N} into \mathcal{G} and \mathcal{P} is motivated by two reasons. First, performing the Park inversion in training results in slow computation speed due to the need for calculating it at each time step using the dynamic variable θ . Second, separating the Park inversion from the training process enables a more direct and informative loss

function, allowing for a clearer understanding of each neural network's behavior.

Substitute the neural block \mathcal{G} defined in (13) into (11):

$$\begin{aligned} \dot{\lambda} &= \mathcal{S}(\lambda, z, r_{s,r}, \mathcal{G}) \\ \lambda &= \mathcal{F}(\mathcal{G}, L_{ls,lr}, L_M) \end{aligned} \quad (15)$$

The physics-informed loss function is derived based on the numerical integration of (15). Without loss of generality, the integration of λ is performed by the modified Euler rule¹:

$$\lambda(t + \Delta t) = \lambda(t) + \frac{\Delta t}{2} \cdot [\dot{\lambda}'(t + \Delta t) + \dot{\lambda}(t)] \quad (16)$$

where $\dot{\lambda}'(t + \Delta t)$ is an estimation of the derivative of λ at time $t + \Delta t$, which is calculated as $\dot{\lambda}'(t + 1) = s(\lambda(t) + \Delta t \cdot \dot{\lambda}(t), z, r_{s,r}, \mathcal{G})$ according to (15); Δt is the time step.

Correspondingly, the loss function for \mathcal{G} is developed as:

$$\begin{aligned} \min_{\theta} L_{\mathcal{G}} &= \text{mean}(\|\Delta\lambda(t)\|_2) \\ \text{s.t. } \Delta\lambda(t) &= \lambda(t) + \frac{\Delta t}{2} \cdot [\dot{\lambda}'(t + \Delta t) + \dot{\lambda}(t)] - \lambda(t + \Delta t) \end{aligned} \quad (17)$$

The loss function in (17) is constructed leveraging both the neural network-based phase-domain IM model and the physics-based $dq0$ -domain IM model, thus compelling the NeuIM to align with the physics laws even without using training data.

Similarly, the training model for \mathcal{P} is developed as:

$$\begin{aligned} \min_{\theta} L_{\mathcal{P}} &= \text{mean}(\|\Delta\hat{i}_s(t)\|_2) \\ \text{s.t. } \Delta\hat{i}_s(t) &= \frac{\Delta t}{2} \cdot \left[\frac{d\hat{i}_s(t + \Delta t)}{dt} + \frac{\hat{i}_s(t)}{dt} \right] + \hat{i}_s(t) - \hat{i}_s(t + \Delta t) \end{aligned} \quad (18)$$

Here, $\Delta\hat{i}_s$ represents the residual of the numerical integration of \hat{i}_s , i.e., the output of the second neural block \mathcal{P} .

The whole process of NeuIM is shown in Fig. 3. The advantages of it lie in: 1) adjustable to different operation scenarios and varied machine parameters because the induction machine parameters (e.g., r_r, r_s, L_M) and boundary conditions (e.g., z) are incorporated into the learning model (see (15)); 2) physically consistent results because the physics laws embedded in the loss function will naturally ensure that the learned model adheres to the governing equations; 3) better generalization with limited data. For hybrid learning, the loss function of \mathcal{G} is:

$$\begin{aligned} \min_{\theta} L_{\text{hybrid},\mathcal{G}} &= L_{\text{physics},\mathcal{G}} + \eta L_{\text{data}} \\ \text{s.t. } L_{\text{data}} &= \text{mean}(\|\hat{i}_s(t) - i_s(t)\|_2) \end{aligned} \quad (19)$$

where $L_{\text{physics},\mathcal{G}}$ stands for the purely physical loss defined in (17) and L_{data} is the loss calculated from training data i_s . η is the percentage of data acquisition. Note that L_{data} will only be calculated for those time points and dimensions that have available measurements. A special case is that if no measurement is available, i_s becomes an empty set and L_{data} correspondingly becomes 0, indicating a purely physics-informed training.

¹Note that the method can be adapted to arbitrary integration algorithms.

B. Static component: grid-forming inverter

In Subsection III-A, although the data-physics hybrid learning is decomposed into multiple neural networks, the learning task within each network, such as in (17), (18), remains straightforward. In contrast, for static components, no framework function is required to split the learning. A single neural network suffices to predict the full-order model, with the trade-off that multiple terms with different physical meanings are calculated within one loss function simultaneously, making it an ideal candidate for evaluating balanced adaptive PIM (BA-PIM).

Consequently, in this subsection, this persistent challenge—the formulation of an effective loss function—is addressed using the example of a grid-forming three-phase inverter. Different from Subsection III-A, this formulation intrinsically encompasses multiple terms, making the allocation of weights a difficult problem. In the proposed BA-PIM, the training process is streamlined automatically.

1) *Physical formulation of an inverter* : Inverters play a fundamental role in the modern power grid by facilitating the transfer of energy from DC voltage sources to AC loads [29]. The topology of a grid-connected system is shown in Fig. 4, where the pink box at the right end represents the connected system. The purple box represents the grid-forming control

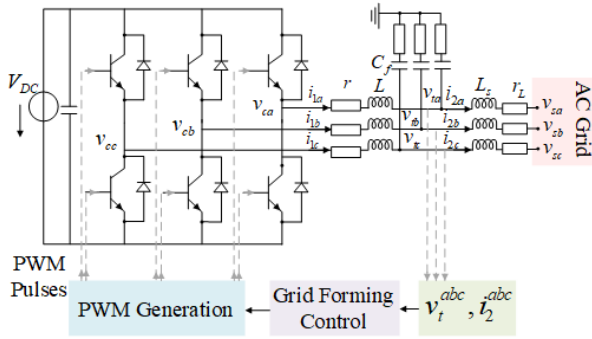


Fig. 4: Topology of grid-connected system.

block. A detailed block diagram of the control structure is presented in Fig. 5. The parameters used are listed in Table V. The power controller consists of the power calculation, $P - \omega$

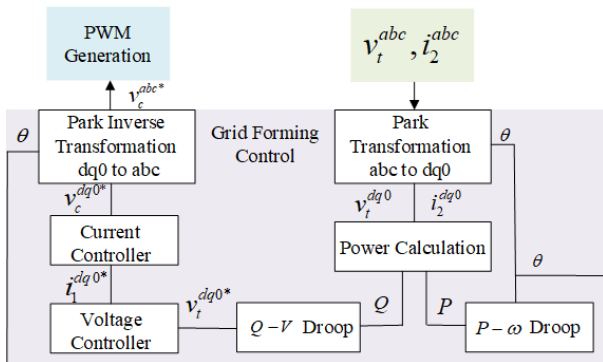


Fig. 5: Block diagram of the grid forming control structure.

ω droop, and $Q - V$ droop control in Fig. 5. The detailed equations are in Appendix A.

2) *Balanced-adaptive physics-informed inverter*: Collecting all the equations from (34) to (36), the ODE for an inverter can be formulated as:

$$\begin{aligned} \frac{dx}{dt} &= \mathcal{Q}(x, u, const) \\ v_c^{dq0} &= \mathcal{R}(x, u) \end{aligned} \quad (20)$$

\mathcal{Q}, \mathcal{R} represents the functions in Appendix A. Define a neural network \mathcal{N} that is capable of predicting \hat{v}_c^{dq0} with inputs of \hat{u} and t . Here $\hat{\cdot}$ denotes the predicted values from \mathcal{N} . Then the final output \hat{v}_c^{abc} can be calculated via inverse Park transformation:

$$\begin{aligned} \hat{v}_c^{dq0}, \hat{x} &= \mathcal{N}(\hat{u}, t) \\ \hat{v}_c^{abc} &= InvPark(\hat{v}_c^{dq0}, \hat{\theta}) \end{aligned} \quad (21)$$

where $\hat{\theta}$ is one of the predicted state variables within \hat{x} .

The core idea of physics-informed learning for PIN-Inverter is to integrate the physical equations (20) in the loss function of training, ensuring the predicted values in (21) satisfy the physical constraints. Following the philosophy in Subsection II-B, the hybrid loss function can be formulated into a physical term and a data-driven term:

$$\mathcal{L} = L_{phy} + \eta L_{data} \quad (22)$$

For the data-driven term L_{data} , define:

$$L_{data} = \|\hat{v}_c^{dq0} - v_c^{dq0}\|_2 + \|\hat{x} - x\|_2 \quad (23)$$

We then derive the physics-informed loss function based on the numerical integration of (20). Without loss of generality, an estimation of \hat{x} is performed by the modified Euler rule:

$$\begin{aligned} \hat{x}'(t + \Delta t) &= \frac{\Delta t}{2} \left[\frac{d\hat{x}(t + \Delta t)}{dt} + \frac{d\hat{x}(t)}{dt} \right] + \hat{x}(t) \\ s.t. \frac{d\hat{x}(t + \Delta t)}{dt} &= A\hat{x}(t + \Delta t) + Bu(t + \Delta t) + const \end{aligned} \quad (24)$$

where $d\hat{x}(t + \Delta t)/dt$ is an estimation of the derivative of \hat{x} at time $t + \Delta t$. It is calculated using the predicted value \hat{x} from the neural network. Δt is the time step. The loss function for L_{dx} is developed as:

$$\begin{aligned} L_{dx} &= mean\|\Delta dx\|_2 \\ s.t. \Delta dx(t) &= \hat{x}'(t + \Delta t) - \hat{x}(t + \Delta t) \end{aligned} \quad (25)$$

Similarly, we define L_v and L_{Cx} as:

$$\begin{aligned} L_v &= mean\|\Delta \hat{v}\|_2, \quad L_{Cx} = mean\|\Delta \hat{C}x\|_2 \\ s.t. \Delta \hat{v} &= \hat{C}x + D\hat{u} - \hat{v}, \quad \Delta Cx = C \cdot \hat{x} - \hat{C}x \end{aligned} \quad (26)$$

Here, $\hat{C}x$ represents an intermediate value predicted by the neural network. Due to the presence of large values in the original matrix C , precision diminishes after normalization. Therefore, the incorporation of L_{Cx} can serve to regularize the term $\hat{C}x$, thereby improving accuracy.

The derivation of L_v takes full advantage of the physical equations in (20). Finally, the physical term L_{phy} , comprising L_v and L_{dx} , L_{Cx} , quantifies the discrepancy between the predicted values from the neural network and the values calculated using the physical equations. Given the number of

terms included in L_{phy} , the balanced and adaptive physics-informed loss is implemented as discussed in Subsection II-C. Losses of the balanced-adaptive PIM-based inverter are first balanced and then optimized as:

$$\begin{aligned} \mathcal{L} &= L_{phy}(\lambda_a, \lambda_b, \lambda_c) + L_{data} \\ \min_{\delta} \max_{\lambda_a, \lambda_b, \lambda_c} \mathcal{L}(\delta, \lambda_a, \lambda_b, \lambda_c) \\ L_{phy} &= \frac{\lambda_a L_v + \lambda_b L_{dx} + \lambda_c L_{Cx}}{\max(L_v, L_{dx}, L_{Cx})} \end{aligned} \quad (27)$$

IV. CASE STUDY

A. Validity of PIM-based induction machine

This subsection verifies the performance of a PIM-based induction machine under various operational conditions and demonstrates its advantages over the data-driven method.

1) *Experiment settings*: PIM-based NeuIM is deployed with Tensorflow 1.5 (Python 3.6) with 2 hidden layers. The ground truth of the IM dynamics is obtained by running the original VBR model in Matlab, which is cross-validated from the results in [26]. The free acceleration and torque change case uses a 3-hp machine, 2500-hp machine is used for the fault case. The test system is an induction machine connected to an infinite bus. Key machine parameters are given in Table I.

The training sets comprise 6 sets of trajectories, encompassing free acceleration, torque change, and fault cases. Note that the goal is to maximize the utilization of limited data, hence the training sets are not extensive. The testing was carried out on 14 distinct sets, with additional parameter changes and noisy measurements. The training time is 0.087s per iteration, in total 5320 iterations for all training data. The computation time of implementing a converged PIM-based induction machine is shown in Table IV.

TABLE I: Induction Machine Parameters.

Parameters	3-hp	2250-hp
r_s	0.435 Ω	0.029 Ω
X_{ls}	0.754 Ω	0.226 Ω
X_M	26.13 Ω	13.04 Ω
X_{lr}	0.754 Ω	0.226 Ω
r_r	0.816 Ω	0.022 Ω
J	0.089 $Kg \cdot m^2$	63.97 $Kg \cdot m^2$
T_B	11.9 $N \cdot m$	8900 $N \cdot m$
Line-to-line Voltage	220 V	2300 V
Poles	4	4

The efficacy of the NeuIM is validated in three scenarios, free acceleration, torque changes, and faults, as specified in Table II. A typical load torque change scenario is shown in Fig. 6a. The mechanical torque T_m changes from 0 to 12 N·m at 2.05s and stays at 12 N·m until 2.5s, then T_m is reversed to -12 N·m, stays till the end. This case is marked ± 12 in Table II. A typical fault case is shown in Fig. 6b, where a three-phase fault is applied at 6.1s and cleared at 6.2s. The IM parameter L_M also changes in testing to show the adaptability of the NeuIM.

2) *Efficacy of the PIM-based induction machine under slow dynamics*: Fig. 7 presents the performance of NeuIM under free acceleration and torque changes. Fig. 7a-7b show the accuracy of predictions from the first neural network \mathcal{G} ;

TABLE II: Data settings.

Scenario	Data set	torque/(N·m)	Voltage/kV	L_M/H
Torque change (3-hp)	training	$\pm 5, \pm 8, \pm 10$	0.22	0.0693
	testing	$\pm 3, \pm 6, \pm 12$	0.22	0.0693
Fault (2500-hp)	training	8900	2.3, 2.5	0.0346
	testing	8900	2.0, 2.2, 2.35	0.0531

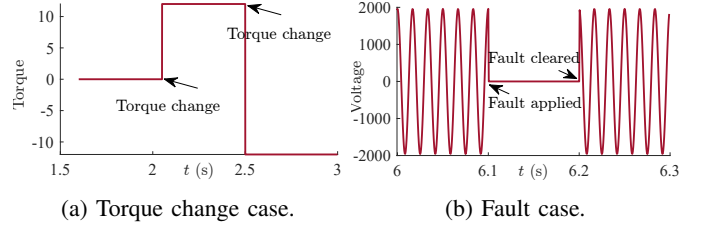


Fig. 6: Scenarios of the training sets.

Fig. 7c-7d show the final results of \mathcal{P} . Trajectories of predicted current i_s^q and the final output of di_s^a/dt demonstrate a perfect match between PIM-based induction machine's results and real dynamics, verifying the accuracy of the PIM-based induction machine in capturing the relatively slow dynamics. Note that this training is purely physics-informed, indicating no ground truth values of i_s^{dq0} , i_s^{abc} are utilized. This underscores its effectiveness in capturing dynamic models solely through physical equations, even in the absence of data.

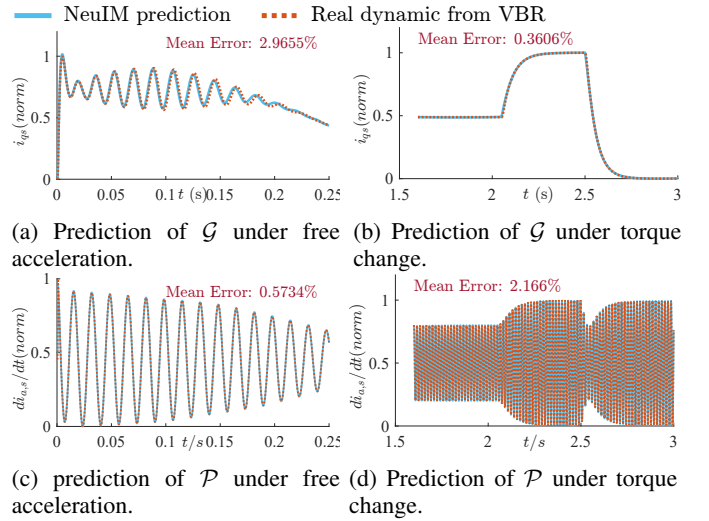


Fig. 7: PIM-based NeuIM performance under free acceleration and torque change.

3) *Efficacy of the PIM-based induction machine under fast dynamics*: A three-phase short circuit is applied at the terminals at 6.1s and cleared at 6.2s. In the training, the parameter L_M is 0.0346 H while in the testing set, L_M is 0.0531 H. Fig. 8c illustrates the performance of the hybrid PIM-based induction machine under different portions of data. For instance, 75% (3:4) hybrid means that 75% of training trajectories have the true values of the outputs of \mathcal{G} , i.e. $i_{s,r}^{dq0}$; thus the loss of these trajectories is $L_{phy} + L_{data}$. For the other 25% of the trajectories where the true values of $i_{s,r}^{dq0}$ are unavailable, the loss of these remaining subsets only consists of L_{phy} . Since the derivatives of currents are not readily

obtained from measurements, the training philosophy for \mathcal{P} is always purely physics-informed.

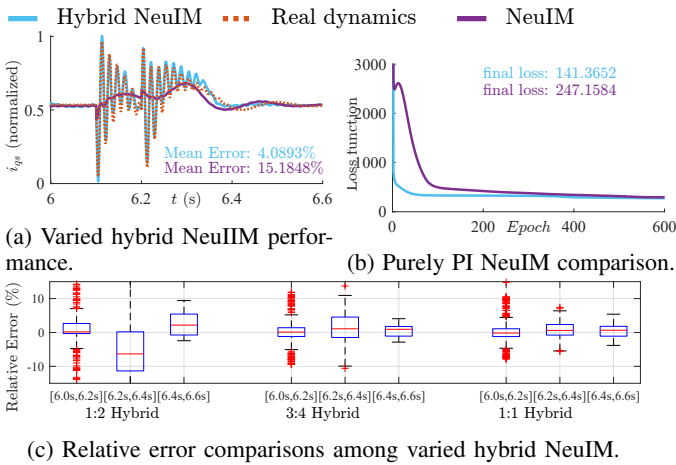


Fig. 8: Performance and comparisons of NeuIM.

From Fig. 8c, it can be drawn that the difficulty for training lies in the post-disturbance period [6.2s,6.4s], especially when the proportion of data is 50% (1:2). The reason lies in the nature of the physical equations governing this problem, as outlined in (15), which involve a set of ordinary differential equations. In scenarios characterized by sudden and rapid changes, certain segments of the trajectories, such as [6.2s,6.4s], exhibit relatively large derivatives or may not be continuous. This makes it challenging for a purely physics-informed neural network to identify optimal solutions.

In such scenarios, Fig. 8b shows that the hybrid NeuIM significantly enhances the convergence speed, particularly in the initial stages of training, while retaining the benefits of physics-informed learning. Fig. 8a shows that 1:1 NeuIM ($\eta = 1$) yields satisfactory results. When the proportion of data vastly exceeds 1:1, the physical loss will be overshadowed by the data-driven loss and is more inclined to data-driven training. In the next subsection, We will discuss the advantages of the hybrid NeuIM with a data-driven approach.

In sum, the PIM-based NeuIM not only delivers high-fidelity solutions but also leverages the underlying physical mechanisms. It explores the data efficiency of PIM with various levels of data availability, including scenarios with no data.

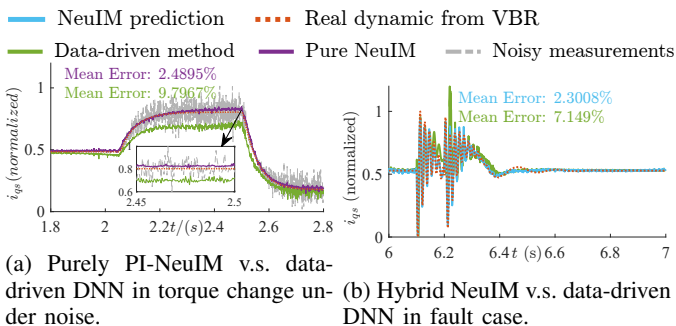


Fig. 9: Comparison between NeuIM and data-driven method.

4) *Comparison with data-driven approach:* For slow dynamics where purely physics-informed NeuIM is used, in

Fig. 9a, 20% of Gaussian noise is added to the measurements. It is observable that the purely data-driven deep neural network (green curve), which has the same structure as NeuIM, has irregular oscillations due to its training with limited data under noise. Meanwhile, NeuIM (purple curve) is more resilient and close to real dynamics (red dotted curve) under noisy measurements (grey curve) with an error rate of less than 3%.

For fast dynamics, in Fig. 9b, it is obvious that hybrid NeuIM achieves a lower mean error rate, showing better generalization ability when facing different fault contingencies.

TABLE III: MSE comparison of methods in IM modeling.

Type	Fault	Torque change
Purely data-driven	0.0386	0.4330
Purely PI NeuIM	0.7352	0.0182
1:1 Hybrid NeuIM	0.0142	0.0158

Table III shows the final results from \mathcal{P} . Hybrid physics-informed NeuIM overshadows the purely data-driven DNN in terms of accuracy, which reveals that under the same training set, NeuIM has a better generalization ability to cope with unseen cases and varied parameters.

For slow transients such as torque change, both NeuIM and hybrid NeuIM beat the data-driven approach. For the fault cases, the hybrid NeuIM outperforms both the data-driven method and the purely physical-informed NeuIM in terms of better convergence rates and lower MSE, with the percentage of data acquisition being 1:1. The data-driven approach, even though it outperforms the pure NeuIM when data is available, cannot grasp the transients completely when one machine parameter changes. In addition, as in Table IV, by checking the overall calculation time, NeuIM is significantly more efficient and its scalability is guaranteed.

TABLE IV: Computation time of VBR ($\Delta t = 0.5ms$) and NeuIM.

Scenario	NeuIM	VBR
Free Acceleration ($T = 1s$)	0.1684s	0.4756s
Torque change ($T = 3.5s$)	0.5514s	1.2751s
Fault ($T = 10s$)	0.5553s (80% hybrid)	2.0727s

B. Efficacy of PIM-based inverter

Following the insight from NeuIM in Subection IV-A3, where the data level between L_{phy} and L_{data} is 1:1, e.g., $\mathcal{L} = L_{phy} + L_{data}$, this section further explores the allocation of weights within L_{phy} by tests on a PIM-based inverter.

1) *Experiment settings:* The case studies are performed on the IEEE 39 bus system. The interface of a Balanced Adaptive (BA)-PIM-based inverter connecting with the rest of the system is illustrated in Fig. 10. The training set consists of 6 scenarios including load change of r_L and short circuit faults, represented by the open switch in Fig. 10. Note that the goal is to maximize the utilization of limited data, hence the training sets are not extensive. The testing was carried out on 20 distinctive cases, where faults happen and clear at different times, and load changes for different levels, randomly ranging between [0.8, 1.2] to the original load.

Training sets were simulated by the detailed full-order physical model via Python 3.7 and were cross-validated from

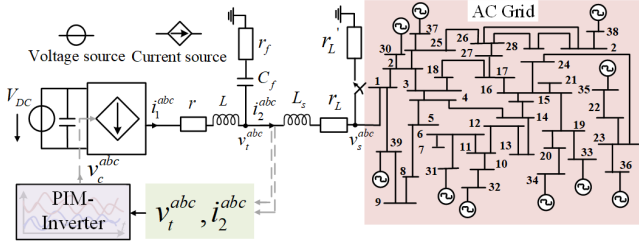


Fig. 10: Interface of PIM-Inverter with IEEE 39 bus system.

TABLE V: Parameters for inverter.

Parameter	Value
$\omega_n, \omega_f, F, V_n$	$2\pi f$ ($f=60$ Hz), 10π , 0.75, 230Kv
r, r_L, r_s, L, L_s	0.1, 16, 0.3, $1.35e-3$, $0.35e-3$
K_p, K_q, K_{pc}	$9.4e-5$, $1.3e-4$, 31.5
K_{ic}, K_{pv}, K_{iv}	8e4, 0.2, 3120

RTDS results. Training and closed-loop testing are developed and implemented in Python 3.7 with Pytorch 1.13. The neural network follows a multi-layer perception structure, which has 2 hidden layers with [128,64] neurons. Key parameters are shown in Table V. The data level follows the percentage 1:1 as stated in Subsection IV-A3.

2) *PIM-based inverter under varied operational conditions:* The dynamic simulation of the system requires assembling the PIM-based inverter model from the rest of the physics model, which is referred to as the closed-loop simulation in the following discussion, where the PIM-based inverter is inserted back into the system in the step-by-step simulation. So the accuracy of the outputs from the neural network directly impacts the results for the next timestep.

Fig. 11 presents the closed-loop performance of the PIM-based inverter under fault and load change. Fig. 11a-11d show the high accuracy of predictions under fault and load change respectively. Trajectories of intermediate variables current i_1^d and i_2^d in Fig. 12 demonstrate a perfect match between the PIM-based inverter's results and real dynamics, verifying the accuracy of PIM-based inverter in capturing the transients.

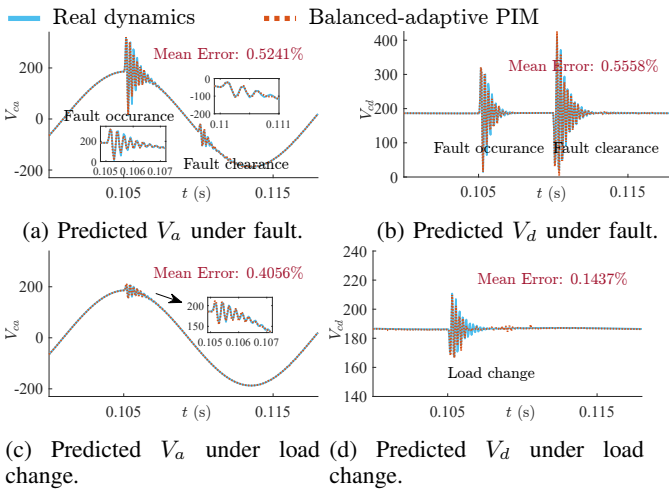


Fig. 11: Voltages of PIM-based inverter under disturbances.

Fig. 13 displays the time-series relative error of predictions made by the PIM-based inverter across 20 scenarios. It

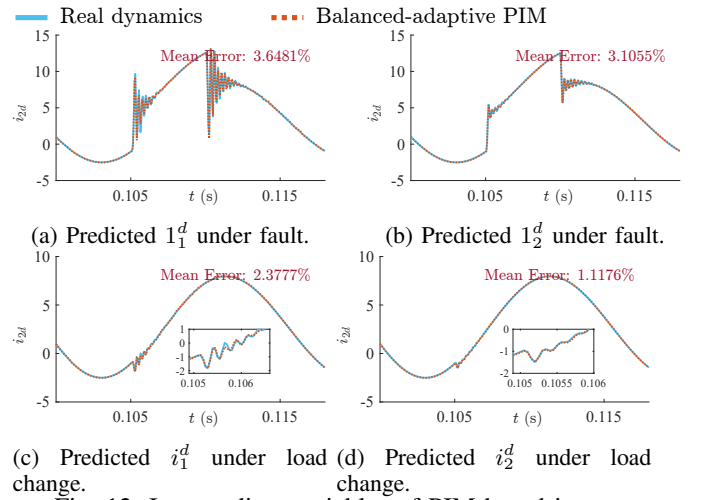


Fig. 12: Intermediate variables of PIM-based inverter.

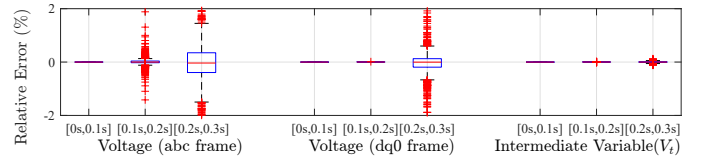


Fig. 13: Error rate of voltages under 20 fault cases.

demonstrates that even in unforeseen circumstances, the PIM-based inverter maintains reasonable error rates throughout the time horizon. This highlights its effectiveness in preserving dynamic behaviors following contingencies and its satisfactory generalization capability beyond the training datasets.

3) *Comparative analysis:* This subsection compares the proposed BA-PIM method with the existing purely data-driven method and a baseline PINN to reveal its necessity and superiority. In Fig. 14, a baseline PINN and a data-driven deep neural network, which share the same neural network structure and training datasets as the proposed method, are tested under a fault case. It is obvious that in Fig. 14a, it is evident that all

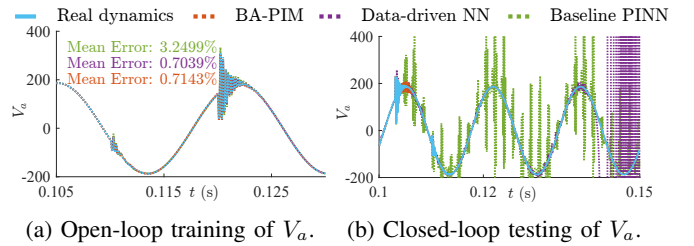


Fig. 14: Comparison of performances via different methods.

three methods achieve satisfactory results during the open-loop training, indicating convergence of the networks. However, in the closed-loop test in Fig. 14b, the baseline PINN (green dotted line) exhibits irregular oscillations and the data-driven method struggles to converge by the end of the trajectory. This discrepancy arises because, during the closed-loop test, the learned neural network interacts with the physical system at each time step. Consequently, even minor residual errors can accumulate over time.

As shown in Fig. 14a and Table VI, baseline PINN has

slightly difficulty in open-loop training, necessitating more training iterations. However, its poor performance in the closed-loop test indicates suboptimal network behavior. The data-driven method is notably sensitive to data quantity and quality, making it unstable when confronted with unforeseen data. From Table VI, it is evident that BA-PIM surpasses the performance of other methods.

TABLE VI: MSE comparison of methods in inverter modeling.

Method	Data-driven	Baseline PINN	BA-PIM
Error Rate	65.9169%	17.8807%	0.6015%
Training iterations	4100	6000	4100
MSE	1.7914e3	76.2240	4.1921

V. CONCLUSION

This paper devises a physics-informed neural modeling (PIM) approach to establish the continuous-time dynamics of power system components by leveraging the component physics knowledge. Case studies of NeuIM show that for slow transients, PIM operates effectively without data, while for fast transients, the data-physics hybrid PIM performs better. An improved Balanced-Adaptive PIM (BA-PIM) reduces the difficulty of determining weights by automatically optimized training. Integrated into a connected system, the PIM-based inverter is effective under various contingencies, surpassing purely data-driven methods and baseline PINNs.

In a nutshell, PIM scales efficiently to large, complex systems and offers a flexible, interpretable, and observable framework. It eliminates the need for extensive EMT trajectories as training samples. The success of PIM marks the first step toward skillfully combining power system transient analysis and artificial intelligence. Each approach has its strengths and weaknesses, but they can complement each other. By exploiting both, the learning-infused EMT simulations are effective while remaining as reliable as the original full-scale model-based EMT simulations.

APPENDIX A

A. Induction machine modeling

The voltage and flux linkage equations in (11) can be expressed as:

$$\begin{aligned}
 v_s^{dq0} &= r_s i_s^{dq0} + \omega \lambda_s^{dq0} + \dot{\lambda}_s^{dq0} \\
 0 &= r_r i_r^{dq} + (\omega - \omega_r) \lambda_r^{dq} + \dot{\lambda}_r^{dq} \\
 \lambda_s^{dq} &= L_{ls} i_s^{dq} + L_M (i_s^{dq} + i_r^{dq}) \\
 \lambda_r^{dq} &= L_{lr} i_r^{dq} + L_M (i_s^{dq} + i_r^{dq}) \\
 \lambda_{0s} &= L_{ls} i_{0s}, \quad \lambda_r^0 = L_{lr} i_r^0, \quad 0 = r_r i_r^0 + \dot{\lambda}_r^0
 \end{aligned} \tag{28}$$

The flux linkage equations can be rearranged as follows:

$$\begin{aligned}
 \lambda_s^q &= L'' i_s^q + \lambda_q'', \quad L_q'' = L_M \frac{\lambda_r^q}{L_{lr}} \\
 \lambda_s^d &= L'' i_s^d + \lambda_d'', \quad L_d'' = L_M \frac{\lambda_r^d}{L_{lr}} \\
 L'' &= L_{ls} + L_M'', \quad L_M'' = \left(\frac{1}{L_M} + \frac{1}{L_{lr}} \right)^{-1}
 \end{aligned} \tag{29}$$

Applying the inverse transformation to

$$\mathbf{v}_s^{abc}(t) = \mathbf{r}_s \mathbf{i}_s^{abc}(t) + \frac{d[\mathbf{L}'' \mathbf{i}_s^{abc}(t)]}{dt} + \mathbf{v}''_s(t) \tag{30}$$

$$\text{where } \mathbf{v}''_s(t) = [\mathbf{K}_s(\theta)]^{-1} \begin{bmatrix} v_g'' \\ v_d'' \\ 0 \end{bmatrix},$$

$$\mathbf{L}''_s = \begin{bmatrix} L_{ls} + \frac{2}{3} L_M'' & -\frac{L_M''}{3} & -\frac{L_M''}{3} \\ -\frac{L_M''}{3} & L_{ls} + \frac{2}{3} L_M'' & -\frac{L_M''}{3} \\ -\frac{L_M''}{3} & -\frac{L_M''}{3} & L_{ls} + \frac{2}{3} L_M'' \end{bmatrix}$$

$$v_d'' = -\omega \lambda_q'' + \frac{L_M'' r_r}{L_{lr}^2} [\lambda_d'' - \lambda_r^d + L_M'' i_s^d] + \frac{L_M''}{L_{lr}} (\omega - \omega_r) \lambda_r^q$$

$$v_q'' = \omega \lambda_d'' + \frac{L_M'' r_r}{L_{lr}^2} [\lambda_q'' - \lambda_r^q + L_M'' i_s^q] - \frac{L_M''}{L_{lr}} (\omega - \omega_r) \lambda_r^d$$

1) *Discrete VBR model*: Based on the trapezoidal rule, (30) can be discretized and rearranged as:

$$\begin{aligned}
 \mathbf{v}_s^{abc}(t) &= \left(\mathbf{r}_s + \frac{2}{\Delta t} \mathbf{L}''_s \right) \mathbf{i}_s^{abc}(t) + \mathbf{v}''_s(t) + \mathbf{e}_h(t) \\
 \mathbf{e}_h(t) &= \left(\mathbf{r}_s - \frac{2}{\Delta t} \mathbf{L}''_s \right) \mathbf{i}_s^{abc}(t - \Delta t) + \\
 &\quad \mathbf{v}''_s(t - \Delta t) - \mathbf{v}_s^{abc}(t - \Delta t)
 \end{aligned} \tag{31}$$

Rewrite (31) and apply the inverse Park transformation, the equivalent circuit for the stator voltage can be written as:

$$\mathbf{i}_s^{abc}(t) = \mathbf{G}_{eq} \mathbf{v}_s^{abc}(t) - \mathbf{h}(t), \quad \mathbf{h}(t) = \mathbf{G}_{eq} [\mathbf{e}_h(t) + \mathbf{e}_{hs}(t)] \tag{32}$$

$$\text{where } \mathbf{K}(t) = [\mathbf{K}_s(\theta(t))]^{-1} \begin{bmatrix} \mathbf{K}_1(t) & 0 \\ 0 & 0 \end{bmatrix} [\mathbf{K}_s(\theta(t))],$$

$$\mathbf{e}_{hs}(t) = [\mathbf{K}_s(\theta(t))]^{-1} \begin{bmatrix} \mathbf{K}_2(t) \\ 0 \end{bmatrix}, \quad \mathbf{G}_{eq} = \left[\mathbf{r}_s + \frac{2}{\Delta t} \mathbf{L}''_s + \mathbf{K}(t) \right]^{-1}$$

$$\begin{aligned}
 \mathbf{K}_2(t) &= A \cdot B \begin{bmatrix} 2 + b_{11} \Delta t & b_{12}(t - \Delta t) \Delta t \\ b_{21}(t - \Delta t) \Delta t & 2 + b_{22} \Delta t \end{bmatrix} \begin{bmatrix} \lambda_{qr}(t - \Delta t) \\ \lambda_{dr}(t - \Delta t) \end{bmatrix} \\
 &\quad + A \cdot B^{-1} \begin{bmatrix} b_{13} \Delta t & 0 \\ 0 & b_{23} \Delta t \end{bmatrix} \begin{bmatrix} i_{qs}(t - \Delta t) \\ i_{ds}(t - \Delta t) \end{bmatrix}
 \end{aligned}$$

$$A = \begin{bmatrix} a_{11} & a_{12} \\ -a_{12} & a_{11} \end{bmatrix}, \quad a_{11} = \frac{L_M'' r_r}{L_{lr}^2} \left(\frac{L_M''}{L_{lr}} - 1 \right)$$

$$a_{12} = \omega_r(t) \frac{L_M''}{L_{lr}}, \quad a_{13} = \frac{L_M'' r_r}{L_{lr}^2}, \quad a_{23} = a_{13}$$

$$B = \begin{bmatrix} 2 - b_{11} \Delta t & -b_{12}(t) \Delta t \\ b_{12}(t) \Delta t & 2 - b_{11} \Delta t \end{bmatrix}, \quad b_{11} = \frac{r_r}{L_{lr}} \left(\frac{L_M''}{L_{lr}} - 1 \right)$$

$$b_{12} = -\omega(t) \omega_r(t), \quad b_{13} = \frac{r_r}{L_{lr}} L_M'', \quad b_{23} = b_{13}$$

For the mechanical part:

$$\begin{aligned}
 T_e &= J \left(\frac{2}{P} \right) \dot{\omega}_r + T_m, \quad \omega_r = \dot{\theta}_r \\
 T_m &= \frac{3P}{4} \cdot (\lambda_{ds} i_{qs} - \lambda_{qs} i_{ds})
 \end{aligned} \tag{33}$$

where T_e is the electromagnetic torque output, J is the inertia of the rotor, T_m is the mechanical torque. θ_r is the electrical angular displacement of the rotor. P is the number of poles.

B. Inverter modeling

The power calculation, P - ω droop and Q - V droop control in Fig. 5 are presented below:

$$\begin{aligned}
 P &= v_t^d i_2^d + v_t^q i_2^q, \quad Q = -v_t^d i_2^q + v_t^q i_2^d \\
 \omega &= \omega_n - k_p \cdot P \cdot \frac{\omega_f}{s + \omega_f}, \quad V = V_n - k_q \cdot Q \cdot \frac{\omega_f}{s + \omega_f}
 \end{aligned} \tag{34}$$

The voltage controller in Fig. 5 can be represented as:

$$\begin{aligned} v_t^{d*} &= V, \quad v_t^{q*} = 0 \\ \frac{d\phi^d}{dt} &= v_t^{d*} - v_t^d, \quad \frac{d\phi^q}{dt} = v_t^{q*} - v_t^q \\ i_1^{d*} &= F i_2^d - \omega_n C_f v_t^d + K_{pv} \cdot (v_t^{d*} - v_t^d) + K_{iv} \phi^d \\ i_1^{q*} &= F i_2^q - \omega_n C_f v_t^q + K_{pv} \cdot (v_t^{q*} - v_t^q) + K_{iv} \phi^q \end{aligned} \quad (35)$$

The current controller is:

$$\begin{aligned} \frac{d\gamma^d}{dt} &= i_1^{d*} - i_1^d, \quad \frac{d\gamma^q}{dt} = i_1^{q*} - i_1^q \\ v_c^{d*} &= -\omega_n \cdot L \cdot i_1^d + K_{pc} \cdot (i_1^{d*} - i_1^d) + K_{ic} \gamma^d \\ v_c^{q*} &= \omega_n \cdot L \cdot i_1^q + K_{pc} \cdot (i_1^{q*} - i_1^q) + K_{ic} \gamma^q \end{aligned} \quad (36)$$

The matrices in (20) are:

$$x = \begin{bmatrix} \omega \\ V \\ \theta \\ \phi^d \\ \phi^q \\ \gamma^d \\ \gamma^q \end{bmatrix}, u = \begin{bmatrix} P \\ Q \\ v_t^d \\ v_t^q \\ i_2^d \\ i_2^q \\ i_1^d \\ i_1^q \end{bmatrix}, \tilde{u} = \begin{bmatrix} v_t^d \\ v_t^q \\ i_2^d \\ i_2^q \\ i_1^d \\ i_1^q \end{bmatrix}, const = \begin{bmatrix} \omega_n \omega_f \\ V_n \omega_f \\ 0 \\ 0 \\ 0 \\ 0 \\ 0 \end{bmatrix}$$

$$A = \begin{bmatrix} -\omega_f & 0 & 0 & 0 & 0 & 0 & 0 \\ 0 & -\omega_f & 0 & 0 & 0 & 0 & 0 \\ 1 & 0 & 0 & 0 & 0 & 0 & 0 \\ 0 & 1 & 0 & 0 & 0 & 0 & 0 \\ 0 & 0 & 0 & 0 & 0 & 0 & 0 \\ 0 & K_{pv} & 0 & K_{iv} & 0 & 0 & 0 \\ 0 & 0 & 0 & 0 & K_{iv} & 0 & 0 \end{bmatrix}$$

$$B = \begin{bmatrix} -k_p \omega_f & 0 & 0 & 0 & 0 & 0 & 0 \\ 0 & -k_q \omega_f & 0 & 0 & 0 & 0 & 0 \\ 0 & 0 & 0 & 0 & 0 & 0 & 0 \\ 0 & 0 & -1 & 0 & 0 & 0 & 0 \\ 0 & 0 & 0 & -1 & 0 & 0 & 0 \\ 0 & 0 & -K_{pv} & -\omega_n C_f & F & 0 & -1 \\ 0 & 0 & \omega_n C_f & -K_{pv} & 0 & F & 0 \end{bmatrix}$$

$$C = \begin{bmatrix} 0 & K_{pc} K_{pv} & 0 & K_{pc} K_{iv} & 0 & K_{ic} & 0 \\ 0 & 0 & 0 & 0 & K_{pc} K_{iv} & 0 & K_{ic} \\ 0 & 0 & 0 & 0 & 0 & 0 & 0 \end{bmatrix}$$

$$D = \begin{bmatrix} -K_{pc} K_{pv} & -\omega_n C_f K_{pc} & K_{pc} F & 0 & -K_{pc} & -\omega_n L \\ \omega_n C_f K_{pc} & -K_{pc} K_{pv} & 0 & K_{pc} F & \omega_n L & -k_{PC} \\ 0 & 0 & 0 & 0 & 0 & 0 \end{bmatrix}$$

REFERENCES

- [1] H. W. Dommel, *EMTP Theory Book*. Univ. of British Columbia, 1996.
- [2] P. Zhang, J. R. Marti, and H. W. Dommel, "Induction machine modeling based on shifted frequency analysis," *IEEE Transactions on Power Systems*, vol. 24, no. 1, pp. 157–164, 2009.
- [3] Y. Zhou and P. Zhang, "Neural electromagnetic transients program," in *2022 IEEE Power & Energy Society General Meeting (PESGM)*, pp. 1–5, IEEE, 2022.
- [4] H. Huang, Y. Lin, Y. Zhou, Y. Zhao, P. Zhang, and L. Fan, "Data-driven modeling of power system dynamics: Challenges, state of the art, and future work," *iEnergy*, vol. 2, no. 3, pp. 200–221, 2023.
- [5] F. Feng, Y. Zhou, and P. Zhang, "Neuro-dynamic state estimation for networked microgrids," *IEEE Transactions on Industry Applications*, pp. 1–10, 2024.
- [6] P. Mishra and P. Zhang, "Physics-informed transient stability assessment of microgrids," *iEnergy*, vol. 2, no. 3, pp. 231–239, 2023.
- [7] S. Brahma, R. Kavasseri, H. Cao, N. R. Chaudhuri, T. Alexopoulos, and Y. Cui, "Real-time identification of dynamic events in power systems using pmu data, and potential applications—models, promises, and challenges," *IEEE Transactions on Power Delivery*, vol. 32, no. 1, pp. 294–301, 2017.
- [8] F. As'ad, P. Avery, and C. Farhat, "A mechanics-informed artificial neural network approach in data-driven constitutive modeling," *International Journal for Numerical Methods in Engineering*, vol. 123, no. 12, pp. 2738–2759, 2022.
- [9] Y. Zhang, et. al., "Solar PLUS: Solar Integration through Physics-Aware Learning Based Ultra-Scalable Modeling and Analytics." <https://www.energy.gov/sites/default/files/2021-12/Day%20%20-%20Speaker%2011%20-%20Peng%20Zhang%20-%20BNL.pdf>, 2021.
- [10] Y. Zhou and P. Zhang, "Neuro-reachability of networked microgrids," *IEEE Transactions on Power Systems*, vol. 37, no. 1, pp. 142–152, 2022.
- [11] G. E. Karniadakis, I. G. Kevrekidis, L. Lu, P. Perdikaris, S. Wang, and L. Yang, "Physics-informed machine learning," *Nature Reviews Physics*, vol. 3, no. 6, pp. 422–440, 2021.
- [12] G. S. Misyris, A. Venzke, and S. Chatzivasileiadis, "Physics-informed neural networks for power systems," in *2020 IEEE Power & Energy Society General Meeting (PESGM)*, pp. 1–5, IEEE, 2020.
- [13] Q. Shen, Y. Zhou, Q. Zhang, S. Maslennikov, X. Luo, and P. Zhang, "Physics-aware neural dynamic equivalence of power systems," *IEEE Transactions on Power Systems*, 2023.
- [14] Q. Shen, Y. Zhou, P. Zhang, H. Zhao, Q. Zhang, S. Maslennikov, and X. Luo, "Scalable neural dynamic equivalence for power systems," *IEEE Access*, pp. 1–1, 2024.
- [15] Z. Fang, "A high-efficient hybrid physics-informed neural networks based on convolutional neural network," *IEEE Transactions on Neural Networks and Learning Systems*, vol. 33, no. 10, pp. 5514–5526, 2022.
- [16] G. D. Palensky P, Cvetkovic M and J. A., "Digital twins and their use in future power systems," *Digital Twin 2022, 1:4* <https://doi.org/10.12688/digitaltwin.17435.2>, 2022.
- [17] L. D. McClenny and U. M. Braga-Neto, "Self-adaptive physics-informed neural networks," *Journal of Computational Physics*, vol. 474, p. 111722, 2023.
- [18] R. M., P. P., and K. G.E., "Physics-informed neural networks: A deep learning framework for solving forward and inverse problems involving nonlinear partial differential equations," *Journal of Computational Physics*, vol. 378, pp. 686–707, 2019.
- [19] S. Markidis, "The Old and the New: Can Physics-Informed Deep-Learning Replace Traditional Linear Solvers?," *arXiv e-prints*, p. arXiv:2103.09655, Mar. 2021.
- [20] A. Samadi, L. Söder, E. Shayesteh, and R. Eriksson, "Static equivalent of distribution grids with high penetration of pv systems," *IEEE Transactions on Smart Grid*, vol. 6, no. 4, pp. 1763–1774, 2015.
- [21] S. Wang, Y. Teng, and P. Perdikaris, "Understanding and mitigating gradient pathologies in physics-informed neural networks," *arXiv preprint arXiv:2001.04536*, 2020.
- [22] K. Tang, X. Wan, and C. Yang, "Das-pinns: A deep adaptive sampling method for solving high-dimensional partial differential equations," *Journal of Computational Physics*, vol. 476, p. 111868, 2023.
- [23] S. Wang, "Respecting causality is all you need for training physics-informed neural networks," in *2022 Fall Eastern Sectional Meeting*, AMS, 2022.
- [24] N. Amiri, S. Ebrahimi, and J. Jatskevich, "Saturable voltage-behind-reactance models of induction machines including air-gap flux harmonics," *IEEE Transactions on Energy Conversion*, 2023.
- [25] L. Wang, J. Jatskevich, and S. D. Pekarek, "Modeling of induction machines using a voltage-behind-reactance formulation," *IEEE Transactions on Energy Conversion*, vol. 23, no. 2, pp. 382–392, 2008.
- [26] S. S. Paul Krause, Oleg Wasynczuk, *Analysis of Electric Machinery and Drive Systems, Third Edition*. 2013 Institute of Electrical and Electronics Engineers, Inc., 2013.
- [27] S. Sudhoff, D. Aliprantis, B. Kuhn, and P. Chapman, "An induction machine model for predicting inverter-machine interaction," *IEEE Transactions on Energy Conversion*, vol. 17, no. 2, pp. 203–210, 2002.
- [28] F. Corcoles, J. Pedra, M. Salichs, and L. Sainz, "Analysis of the induction machine parameter identification," *IEEE Transactions on Energy Conversion*, vol. 17, no. 2, pp. 183–190, 2002.
- [29] D. B. Rathnayake, M. Akrami, C. Phurailatpam, S. P. Me, S. Hadavi, G. Jayasinghe, S. Zabihi, and B. Bahrani, "Grid forming inverter modeling, control, and applications," *IEEE Access*, vol. 9, pp. 114781–114807, 2021.